Constraining the bright-end of the UV luminosity function for z 7-9 galaxies: results from CANDELS/GOODS-South

Article (Published Version)

Monthly Notices
of the
ROYAL ASTRONOMICAL SOCIETY

MNRAS **429,** 150–158 (2013) doi:10.1093/mnras/sts325

Constraining the bright-end of the UV luminosity function for $z \approx 7$–9 galaxies: results from CANDELS/GOODS-South

Silvio Lorenzoni,[1]⋆ Andrew J. Bunker,[1] Stephen M. Wilkins,[1] Joseph Caruana,[1] Elizabeth R. Stanway[2] and Matt J. Jarvis[1,3,4]

[1]*Department of Physics, University of Oxford, Denys Wilkinson Building, Keble Road, Oxford OX1 3RH*
[2]*Department of Physics, University of Warwick, Coventry CV4 7AL*
[3]*Centre for Astrophysics, Science & Technology Research Institute, University of Hertfordshire, Hatfield, Herts AL10 9AB*
[4]*Physics Department, University of the Western Cape, Cape Town, 7535, South Africa*

Accepted 2012 October 30. Received 2012 September 20; in original form 2012 June 18

ABSTRACT

The recent *Hubble Space Telescope* near-infrared imaging with the Wide-Field Camera #3 (WFC 3) of the Great Observatories Origins Deep Survey South (GOODS-S) field in the Cosmic Assembly Near-infrared Deep Extragalactic Legacy Survey (CANDELS) programme covering nearly 100 arcmin^2, along with already existing Advanced Camera for Surveys optical data, makes possible the search for bright galaxy candidates at redshift $z \approx 7$–9 using the Lyman break technique. We present the first analysis of z'-drop $z \approx 7$ candidate galaxies in this area, finding 19 objects. We also analyse Y-drops at $z \approx 8$, trebling the number of bright ($H_{\rm AB} < 27$ mag) Y-drops from our previous work, and compare our results with those of other groups based on the same data. The bright high-redshift galaxy candidates we find serve to better constrain the bright end of the luminosity function at those redshift, and may also be more amenable to spectroscopic confirmation than the fainter ones presented in various previous work on the smaller fields (the *Hubble Ultra Deep Field* and the WFC 3 Early Release Science observations). We also look at the agreement with previous luminosity functions derived from WFC 3 drop-out counts, finding a generally good agreement, except for the luminosity function of Yan et al. at $z \approx 8$, which is strongly ruled out.

Key words: galaxies: evolution – galaxies: formation – galaxies: high-redshift – galaxies: starburst – ultraviolet: galaxies.

1 INTRODUCTION

Thanks to the installation of Wide Field Camera 3 (WFC3) on the *Hubble Space Telescope* (*HST*) in 2009 summer, the search for star-forming galaxies at redshifts $z \geq 7$ with the Lyman break technique (see Section 3) has become possible with the infrared channel of the WFC 3 and led to the discovery of several galaxy candidates at $z \approx 7$–10. From these candidates, we can determine the rest-frame UV luminosity function (LF) at these redshifts (Bunker et al. 2010; Bouwens et al. 2011; Lorenzoni et al. 2011; Wilkins et al. 2011a), an important tool in understanding the star formation history of the Universe, and also crucial to addressing the role of star-forming galaxies in reionization. These works show a broad agreement on the clear LF evolution from $z = 6$ (and below) to $z = 7$ with the characteristic luminosity L^* fainter at higher redshifts, and suggest further evolution at even higher redshifts ($z \approx 8$–10), although based on fewer candidates. The wealth of WFC 3 data on the Great Observatories Origins Deep Survey South (GOODS-S) area recently obtained by the Cosmic Assembly Near-infrared Deep Extragalactic Legacy Survey (CANDELS; Grogin et al. 2011; Koekemoer et al. 2011), covering an area twice as large as the area surveyed in our previous papers, allows us to put better constraints on the bright end of the UV LF at $z \approx 7$–9. The larger field now available also allows the identification of brighter sources, which may be more amenable to spectroscopic follow-up. The fact that these new WFC 3 images coincide with existing deep Advanced Camera for Surveys (ACS) optical images is critical in rejecting potential interlopers – the ACS filters lie below the Lyman limit and hence any detection at short wavelength will reject low redshift contaminants. This is a luxury not afforded to recent pure-parallel surveys for high-redshift drop-outs like the Hubble Infrared Pure Parallel Imaging Extragalactic Survey (HIPPIES; Yan et al. 2011) and the Brightest of Reionizing Galaxies (BoRG) survey (Trenti et al. 2011; Bradley et al. 2012). In this paper, we present for the first time a list of z'-drops at $z \approx 7$ drawn from the large CANDELS field of GOODS-S. We also present our selection of $z \approx 8$ Y-drops in this field, and compare this with recent independent analyses of

⋆E-mail: Silvio.Lorenzoni@astro.ox.ac.uk

Table 1. The total exposure time (in ks) is listed for each WFC3 filter used in this study for both CANDELS 'wide' and 'deep' fields. In parenthesis, the average depth for each filter over the area listed is shown. These are 5σ limits calculated in apertures of 0.6 arcsec diameter, corrected as described in the text for aperture loss and reddening.

Field ID	WFC3 exposure times in ks (5σ depth, AB mag)			Area
	Y band	*J* band	*H* band	(arcmin^2)
CANDELS deep	8.1 (27.8)	7.4 (27.3)	7.7 (27.2)	62.9
CANDELS wide	2.7 (26.8)	2.1 (26.9)	2.1 (26.6)	32.8

CANDELS *Y*-drops in GOODS-S by Oesch et al. (2012) and Yan et al. (2012).

This paper is organized as follows. In Section 2, we outline the *HST* observations with WFC 3 and the data reduction, and in Section 3 we describe our colour selection to recover high-redshift Lyman break galaxies, and compare our sample with those from other studies. In Section 4, with discuss the UV LF derived from the new data. Our conclusions are presented in Section 5. Throughout, we adopt the standard concordance cosmology of $\Omega_{\rm M} = 0.3$, $\Omega_\Lambda = 0.7$ and use $H_0 = 70$ km s^{-1} Mpc^{-1}. All magnitudes are on the AB system (Oke & Gunn 1983).

2 OBSERVATIONS AND DATA REDUCTION

2.1 Observations

In this paper, we analyse images from WFC 3 on *HST* taken in the *F*105*W*, *F*125*W* and *F*160*W* filters, corresponding approximately to the near-infrared *Y*, *J* and *H* bands. The data come from the *HST* programmes GO-12060, GO-12061 and GO-12062 in the CANDELS programme (PI: S. Faber; see Grogin et al. 2011; Koekemoer et al. 2011), covering the areas of the GOODS-S field (Giavalisco et al. 2004) not covered by the Early Release Science (ERS) programme GO/DD-11359 (PI: R. O'Connell; see Wilkins et al. 2010). The area is divided into a 'deep' field, measuring ∼63 arcmin^2 with three orbits in each Y_{105w}, J_{125w} and H_{160w} filters, and a 'wide' field with one orbit per filter over an area of ∼33 arcmin^2 (the areas quoted refer to the deepest area where the coverage has the maximum number of overlapping frames). Extensive ACS imaging has been carried in these areas in previous years (Giavalisco et al. 2004; Beckwith et al. 2006) in the *b* (*F*425*W*), *v* (*F*606*W*), *i* (*F*775*W*) and *z*′ (*F*850*LP*) filters, allowing us to confidently use the Lyman break technique to select likely high-redshift star-forming galaxies.

The infrared channel of WFC 3 was used, which is a Teledyne 1014 × 1014 pixel HgCdTe detector (a 10-pixel strip on the edge is not illuminated by sky and used for pedestal estimation), with a field of view of 123 × 136 arcsec^2. The data were taken in 'MULTIACCUM' mode using SPARSAMPLE100, which non-destructively reads the array every 100 seconds. These repeated non-destructive reads of the infrared array allow gradient fitting to obtain the count rate ('sampling up the ramp') and the flagging and rejection of cosmic ray strikes. In Table 1, we list the exposure time for both the 'deep' and 'wide' fields for each spectral band.

2.2 Data reduction

Data reduction is performed as described in our previous papers (Lorenzoni et al. 2011; Wilkins et al. 2011a). We used the IRAF.STSDAS pipeline `calwfc3` to calculate the count rate and reject cosmic rays, then MULTIDRIZZLE (Koekemoer et al. 2003) to combine exposures taking account of the geometric distortions and mapping on to an output pixel size of 0.06 arcsec pixel^{-1} from an original 0.13 arcsec pixel^{-1}, which corresponds to a 2 × 2 block averaging of the GOODSv2.0 ACS drizzled images in *b*, *v*, *i* and *z*′ bands. We used a MULTIDRIZZLE pixel fraction of 0.8 for the 'deep' area and 1.0 for the 'wide' area to recover some of the undersampling. We used our own reduction of all the WFC3 data for the CANDELS GOODS-S 'wide' area and of the *Y*-band data of the 'deep' region. For the *J* and *H* bands covering the 'deep', we used the reduced single epoch images made available by the CANDELS team[1] and co-added these together with inverse-variance weighting (i.e. weighting each pixel by its exposure time).

For WFC3, we use the zero-points reported on http://www.stsci.edu/hst/wfc3/phot_zp_lbn, last updated in 2011 January, where the zero-points are 26.27, 26.25 and 25.96 for *F*105*W*, *F*125*W* and *F*160*W*.

We perform photometry using fixed apertures of 0.6 arcsec diameter, and introduce an aperture correction to account for the flux falling outside of the aperture. This correction was determined to be ≈0.2–0.25 mag in WFC3 from photometry with larger apertures on bright but unsaturated point sources. For the ACS images, the better resolution and finer pixel sampling require a smaller aperture correction of ≈0.1 mag. All the magnitudes reported in this paper have been corrected to approximate total magnitudes (valid for compact sources), and we have also corrected for the small amount of foreground Galactic extinction towards these fields using the *COBE*/DIRBE and *IRAS*/ISSA dust maps of Schlegel, Finkbeiner & Davis (1998). The optical reddening is $E(B-V) = 0.009$, equivalent to extinctions of $A_{850lp} = 0.012$, $A_{105w} = 0.010$, $A_{125w} = 0.008$ and $A_{160w} = 0.005$.

2.3 Construction of catalogues

To perform the candidate selection, we used the SExtractor photometry package (Bertin & Arnouts 1996), version 2.5.0. For *Y*-drops (objects clearly detected in the WFC3 *J* band but with minimal flux in the *Y* band and ACS images), apertures were 'trained' in the *H*-band image, and running SExtractor in dual-image mode those apertures were used to measure the flux in the same locations in the *Y*- and *J*-band images. For each waveband, we used a weight image derived from the exposure map. The *z*′-drop selection was done from catalogues trained in the *J* band rather than in the *H* band

Tables 2 and 3 present our photometry of *z*′- and *Y*-drops from SExtractor. The MULTIDRIZZLE geometric transformation and image re-gridding produces an output where the noise is highly correlated, hence measuring the standard deviation in blank areas of the final drizzled image will underestimate the noise (e.g. Casertano et al.

[1] See http://candels.ucolick.org/data_access/GOODS-S.html.

Table 2. z'-band drop out candidate at $z \approx 7$ meeting either of the selection criteria described. Objects are ordered by apparent J_{AB} magnitude. Where quoted, limits are 1σ.

ID	RA (J2000)	Dec. (J2000)	$z \approx 7$ z_{AB}	Y_{AB}	J_{AB}	H_{AB}	$(z-Y)_{AB}$	$(Y-J)_{AB}$	β
GS.D-zD1	03:32:55.930	−27:49:38.59	26.98 ± 0.21	26.01 ± 0.044	25.87 ± 0.071	26.25 ± 0.15	0.97	0.14	-3.63 ± 0.74
GS.D-zD2[1]	03:32:37.181	−27:48:56.68	28.88 ± 0.74	26.52 ± 0.043	26.34 ± 0.074	26.46 ± 0.12	2.36	0.18	-2.51 ± 0.64
GS.D-zD3[1, 2]	03:32:08.130	−27:46:40.88	>28.49	26.85 ± 0.12	26.37 ± 0.10	26.39 ± 0.15	>1.64	0.48	-2.09 ± 0.82
GS.D-zD4[1]	03:32:36.006	−27:44:41.74	>28.26	26.57 ± 0.067	26.39 ± 0.085	26.52 ± 0.14	>1.69	0.18	-2.56 ± 0.74
GS.D-zD5	03:32:25.447	−27:50:53.36	27.76 ± 0.33	26.76 ± 0.094	26.46 ± 0.084	26.44 ± 0.12	1.0	0.3	-1.91 ± 0.67
GS.D-zD6	03:32:09.583	−27:46:32.06	28.01 ± 0.42	26.99 ± 0.13	26.64 ± 0.11	26.01 ± 0.10	1.02	0.35	0.70 ± 0.73*
GS.W-zD1	03:32:57.390	−27:53:21.77	27.51 ± 0.25	26.56 ± 0.18	26.67 ± 0.16	26.84 ± 0.24	0.95	−0.11	-2.7 ± 1.2
GS.W-zD2	03:32:36.729	−27:54:42.12	27.35 ± 0.21	26.59 ± 0.17	26.77 ± 0.14	26.58 ± 0.17	0.76	−0.18	-1.19 ± 0.94
GS.D-zD7	03:32:36.240	−27:46:31.37	28.51 ± 0.65	27.26 ± 0.12	26.82 ± 0.11	26.78 ± 0.15	1.25	0.44	-1.83 ± 0.85
GS.D-zD8[1]	03:32:40.693	−27:44:16.72	>28.09	27.02 ± 0.11	26.83 ± 0.12	26.71 ± 0.16	>1.07	0.19	-1.49 ± 0.91
GS.D-zD9[1]	03:32:28.859	−27:49:12.63	>28.35	27.18 ± 0.12	26.89 ± 0.14	26.88 ± 0.20	>1.17	0.29	-1.96 ± 1.10
GS.D-zD10[1]	03:32:27.916	−27:45:42.72	>29.28	27.24 ± 0.17	26.9 ± 0.14	27.80 ± 0.47	>2.04	0.34	-5.8 ± 2.1*
GS.D-zD11[1]	03:32:19.938	−27:47:10.57	29.01 ± 1.05	27.04 ± 0.10	26.95 ± 0.13	27.59 ± 0.35	1.97	0.09	-4.7 ± 1.6
GS.D-zD12[1]	03:32:47.638	−27:48:29.21	28.98 ± 0.93	27.17 ± 0.11	27.07 ± 0.15	27.66 ± 0.39	1.81	0.1	-4.5 ± 1.8
GS.D-zD13	03:32:12.512	−27:47:56.86	28.12 ± 0.37	27.22 ± 0.12	27.14 ± 0.16	27.87 ± 0.46	0.9	0.08	-5.1 ± 2.1
GS.D-zD14[1]	03:32:37.230	−27:45:38.41	28.05 ± 0.44	27.02 ± 0.10	27.15 ± 0.15	27.36 ± 0.26	1.03	−0.13	-2.9 ± 1.3
GS.D-zD15[1]	03:32:30.793	−27:50:27.19	>29.03	27.46 ± 0.17	27.17 ± 0.15	27.56 ± 0.32	>1.57	0.29	-3.7 ± 1.6
GS.D-zD16	03:32:16.057	−27:47:57.72	28.09 ± 0.44	27.3 ± 0.13	27.21 ± 0.16	27.70 ± 0.37	0.79	0.09	-4.1 ± 1.8
GS.D-zD17	03:32:35.067	−27:46:34.96	28.35 ± 0.52	27.51 ± 0.15	27.22 ± 0.15	27.89 ± 0.44	0.84	0.29	-4.8 ± 2.0*

[1]In W11 selection.; [2]not selected using B11 criteria.; *outside the colour–colour selection window employed by Wilkins et al. (2011b) for a clean selection of z-drops for analysis of spectral slope, β.

Table 3. Y-band drop out candidate at $z \approx 8$ meeting either of the selection criteria described. Objects are ordered by apparent H_{AB} magnitude.

ID	RA	Dec.	$z \approx 8$ Y_{AB}	J_{AB}	H_{AB}	$(Y-J)_{AB}$	$(J-H)_{AB}$	B11	L11
GS.D-YD1	03:32:48.921	−27:47:07.36	27.0 ± 0.11	26.18 ± 0.063	26.17 ± 0.077	0.82	0.01	✓	
GS.D-YD2	03:32:14.135	−27:48:28.96	28.18 ± 0.3	26.94 ± 0.12	26.8 ± 0.13	1.24	0.14	✓	✓
GS.D-YD3	03:32:25.330	−27:48:54.07	27.18 ± 0.11	26.59 ± 0.086	26.9 ± 0.13	0.59	−0.31	✓	
GS.D-YD4	03:32:44.018	−27:47:27.23	27.8 ± 0.19	27.01 ± 0.13	26.97 ± 0.16	0.79	0.04	✓	
GS.D-YD5	03:32:40.257	−27:44:09.84	27.61 ± 0.18	27.09 ± 0.14	27.02 ± 0.16	0.52	0.07	✓	
GS.D-YD6	03:32:20.979	−27:48:53.46	29.04 ± 0.64	27.0 ± 0.13	27.05 ± 0.16	2.04	−0.05	✓	✓

2000). As in our previous work, we have corrected the magnitude errors returned by SExtractor using our 'true noise frames', combinations of the data obtained without using multidrizzle and hence without correlation between adjacent pixels, to determine the scaling factor (typically SExtractor underestimated the magnitude errors by a factor of ≈2 for pixfrac=0.8 used for most of our data). We also measure the correlated noise (the standard deviation of the background counts) in the drizzled image mosaics which we use for our source detection and photometry, and use the relations in equation (A13) of Casertano et al. (2000) to introduce a correction factor which depends on the output pixel scale and the size of the 'droplet' in the drizzling procedure ('pixfrac'). We generally found good agreement (at the 0.05 mag level) with our sensitivity measurements using the true-noise frames. The errors displayed in Tables 2 and 3 are the corrected output from SExtractor

3 CANDIDATE SELECTION

Identification of candidates is achieved using the Lyman break technique (e.g. Steidel et al. 1996), where a large colour decrement is observed between filters either side of Lyman α in the rest-frame of the galaxy. At $z > 6$, the flux decrement comes principally from the large integrated optical depth of the intervening absorbers (the Lyman α forest).

At $z \approx 8$–9, the location of the Lyman α break is redshifted to ∼1.1 μm – the WFC3 Y_{105w} and J_{125w} are suitably located such that a $7.6 < z < 9.8$ star-forming galaxy will experience a significant flux decrement between these two filters, while for $z \approx 7$ the break lies at ∼1 μm, between filters WFC3 Y_{105w} and ACS z_{850lp}, with a redshift range of $6.5 < z < 8.0$ (see Fig. 1). The selection efficiency drops at the extremes of these ranges.

3.1 Selection criteria

Our photometrically selected Lyman break sample suffers from contamination due to photometric scatter and interlopers (in particular L- and T-type dwarf stars and red galaxies at intermediate redshift). To discriminate candidates from these interlopers, we use the photometric data from another filter at wavelengths longer than the break, J_{125w} for z'-drops and H_{160w} for Y-drops and impose limitations on the $z_{850lp} - Y_{105w}$ and $J_{125w} - H_{160w}$ colours (respectively) as well, drawing a selection window in the colour–colour diagram that excludes most of the contaminants (Fig. 2).

In this work, we present objects within the colour–colour windows we selected and with detections of at least 5σ in the two bands

Table 4. We list here candidates identified by O12 and Y12, second and third column, respectively, and match them with ours when possible (first column) or give the reason why we do not find them (fourth column).

Lorenzoni '12	Oesh '12	Yan '12	Class
GS.D-YD1	–	064	
GS.D-YD2	CANDY-2141348289	–	
GS.D-YD3	CANDY-2253348542	–	
GS.D-YD4	CANDY-2440247273	–	
GS.D-YD5	–	107	
GS.D-YD6	CANDY-2209848535	–	
–	CANDY-2499448181	048	O
–	CANDY-2320345371	–	W
–	CANDY-2209651371	–	O
–	CANDY-2350049216	035	F
–	CANDY-2192147298	–	?
–	CANDY-2181852456	–	F
–	CANDY-2379552208	–	F
–	CANDY-2408551569	–	F
–	–	100	O
–	–	094	F
–	–	043	F
–	–	085	F, W

F – Object too faint in J and/or H band for our selection criteria.
O – Detection of more than 2 σ in at least one of the optical bands.
W – Object outside our colour–colour selection windows.
? – Object not picked up by SExtractor.

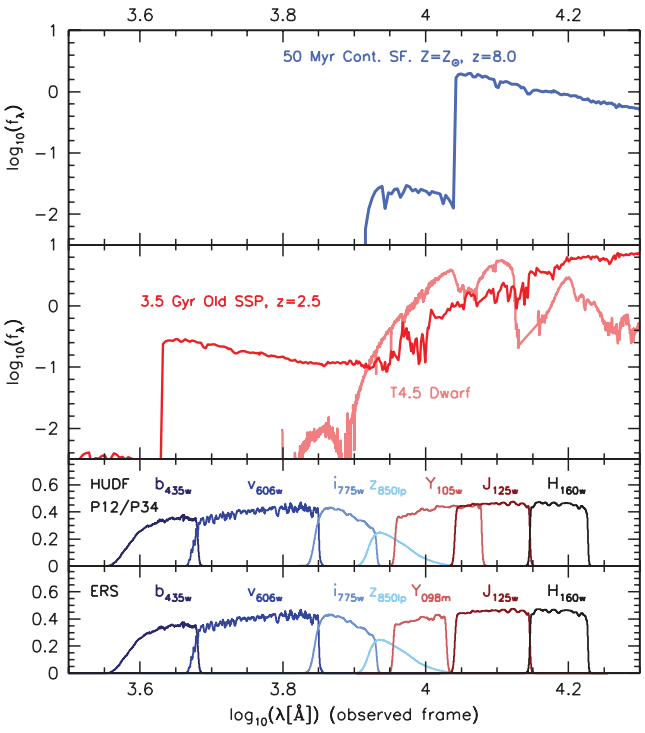

Figure 1. Top panel: model (from the Starburst99; Leitherer et al. 1999) spectral energy distribution (SED) of a redshifted $z = 8$ star-forming galaxy. Middle panel: potential contaminants – observed SED of a low-mass dwarf star (class: *T*4.5; Knapp et al. 2004) together with the model (Starburst99) SED of a 3.5 Gyr single-aged stellar population at $z = 2.5$. The bottom two panels show the transmission functions of the combination of filters available to each field.

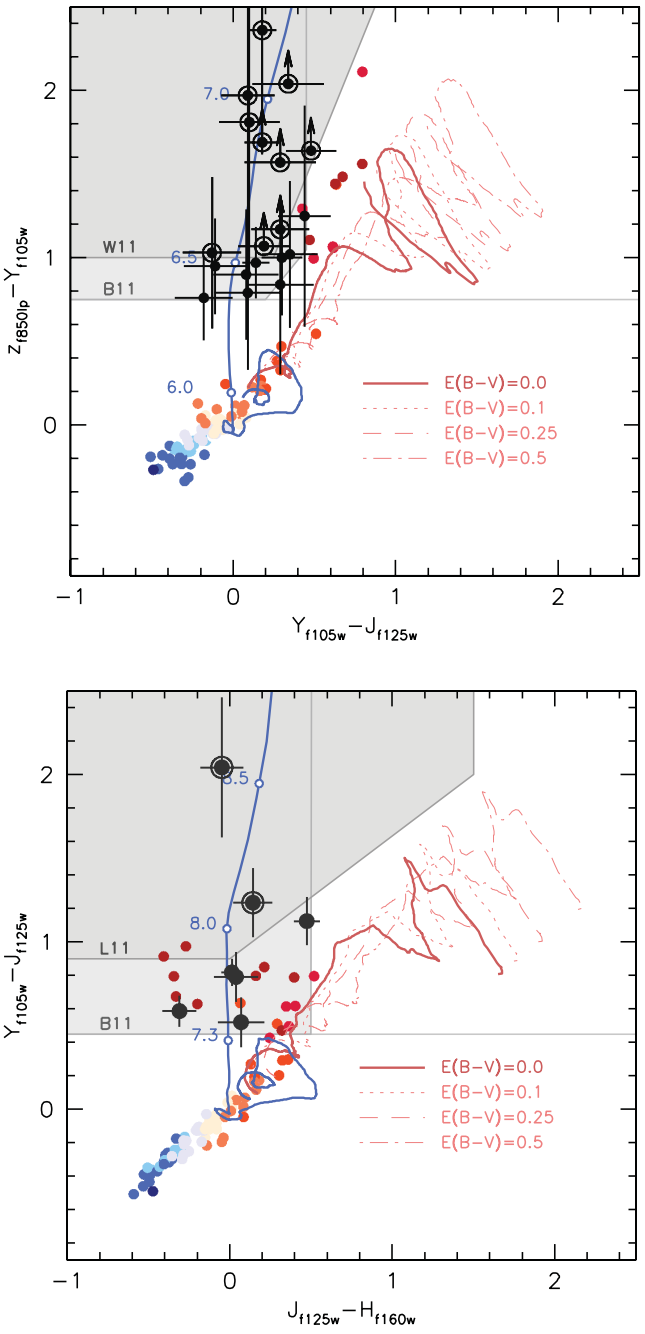

Figure 2. Colour–colour diagrams for both z'-drops (top) and Y-drops (bottom). The shaded areas are the selection windows used, defined in Section 3.1 (light shading for the B11z and B11Y selection windows, darker shading for W11 and L11). The objects we found are shown as grey dots (objects not meeting any of the colour–colour windows we are considering), black dots (objects in B11z or B11Y) and black circled dots (objects meeting W11 or L11). The coloured dots denote the position of potential L and T dwarfs stars contaminants. The solid red line shows the colours that lower redshift galaxies (modelled as an instantaneous burst of star formation at $z = 20$ and no dust) would have, and the dotted, dashed and dot–dashed lines show this low-redshift template with reddenings of $E(B - V) = 0.1$, 0.25 and 0.5, respectively. The blue line is the predicted path taken by high-redshift galaxies (constant star formation from $z = 20$, no dust). For the red and blue tracks, numbers in correspondence with open circles indicate the redshift.

at wavelengths longer than the Lyman α break. Even though the selection windows rule out most of the intrinsically red interlopers, these can still be included in our selection because of photometric scatter. To minimize this contamination, all objects with a $>2\sigma$ detection in any of the b_{435w}, v_{606w} and i_{775lp} (below the Lyman limit) are classified as contaminants, ruling out in this way lower redshift red galaxies, which we expected to faintly detect in the optical bands (see Fig. 1).

Various colour selection windows have been proposed in the literature to remove contaminants and select high-redshift Lyman break galaxies. In this paper, we use the criteria we derived previously for the z'-drops at $z \approx 7$ (Wilkins et al. 2011a, hereafter W11):

$$(z_{850lp} - Y_{105w}) > 1.0,$$
$$(z_{850lp} - Y_{105w}) > 2.4 \times (Y_{105w} - J_{125w}) + 0.9,$$
$$(Y_{105w} - J_{125w}) < 1.0,$$

and for the Y-drops at $z \approx 8$ (Lorenzoni et al. 2011, hereafter L11):

$$(Y_{105w} - J_{125w}) > 0.9,$$
$$(Y_{105w} - J_{125w}) > 0.73 \times (J_{125w} - H_{160w}) + 0.9,$$
$$(J_{125w} - H_{160w}) < 1.5.$$

We also derive a list of candidates obeying the colour cuts proposed by Bouwens et al. (2011) for these redshifts (we label these Bouwens et al. criteria B11z for $z \approx 7$ and B11Y for $z \approx 8$ hereafter). This will allow for an easier comparison of candidates, and to investigate the effect of different selection windows on the derivation of an LF. For detections of less than 1σ in the z' or Y band, we quote a 1σ limit based on the noise and measured flux within the aperture.

3.1.1 z′-drops

In the 'deep' area, we find 17 objects meeting our selection criteria (see Fig. 2, top panel). Of these, 16 candidates meet the B11z selection window, while 10 meet W11 (nine of which also match the B11z window). One of these objects is UDFz-4256656 from Bouwens et al. (2011) in the *Hubble Ultra Deep Field* (HUDF) field. In the 'wide' area, two objects meet the B11z window (GS.W-zD1 and GS.W-zD2), and none falls within the W11 colour selection. Images of the z'-drops meeting the selection criteria (B11z and/or W11) are shown in Fig. 3. Having three filters longwards of the break, it is possible to determine the UV spectral slope for the z'-drop candidates: the Y-band filter could be affected by either the Lyman break or Lyman α emission, or both, so the J and H bands are necessary to have 'clean' information on the UV slope. As in Wilkins et al. (2011b), β is determined from the $(J_{125w} - H_{160w})$ colour by the relation $\beta = 4.28 \times (J_{125w} - H_{160w}) - 2.0$, which assumes that the slope is represented exactly by a power law. The β values are listed in Table 2: as already observed by Bunker et al. (2010), Wilkins et al. (2011b) and Bouwens et al. (2010), the UV slopes of high-redshift galaxy candidates are very blue ($\beta \sim -2$), with fainter objects being bluer than the brighter. Note that the error bars for faint candidates, due to photometric scatter, are considerable.

3.1.2 Y*-drops*

In the CANDELS 'deep' area (Table 3), two objects meet the L11 colour selection (Fig. 4), both of which are included in the six objects selected with the B11Y criteria (Fig. 2 , bottom panel). We did not find any Y-drop candidate in CANDELS 'wide' area.

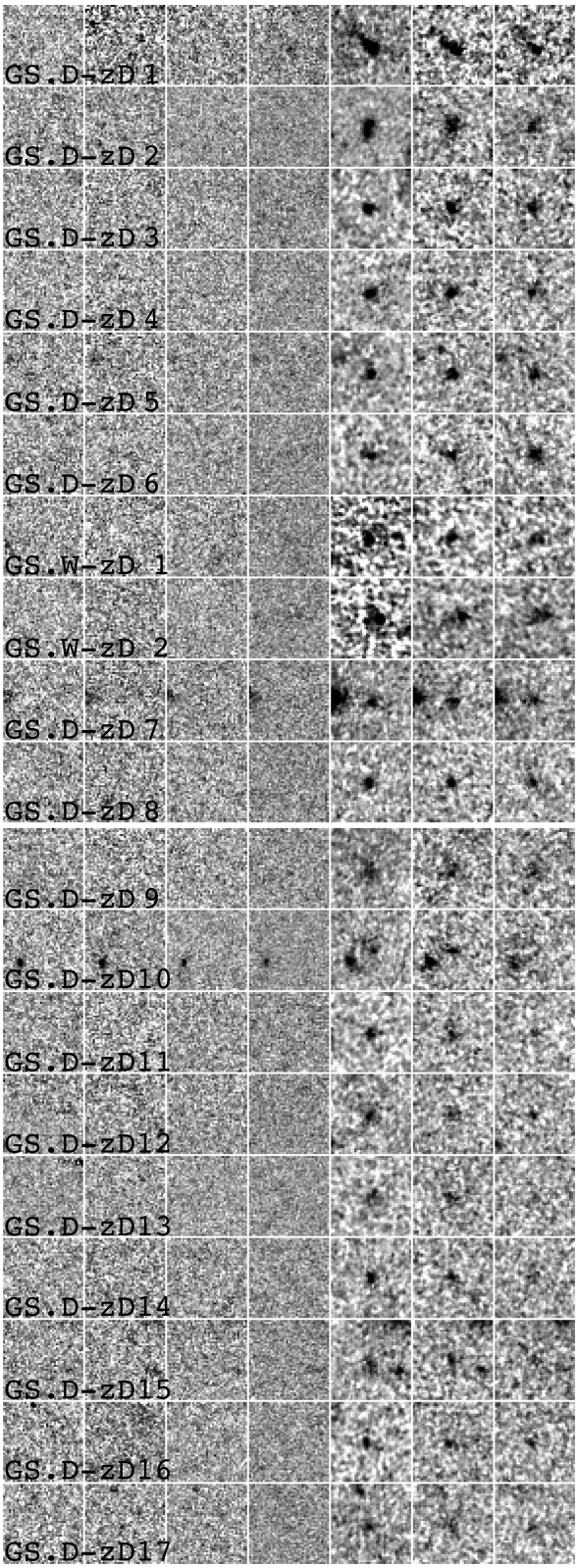

Figure 3. 2.4×2.4 arcsec^2 *bvizYJH* thumbnail images of potential $z \approx 7$ objects meeting our selection criteria in CANDELS GOODS-South field, ordered by J-band magnitude (brightest at the top).

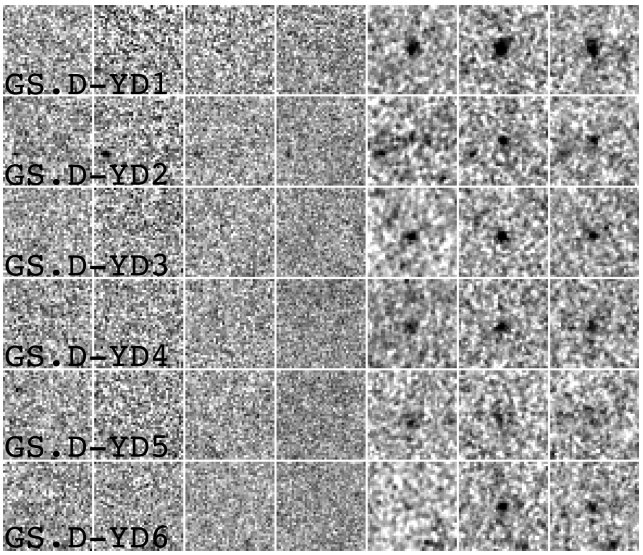

Figure 4. 2.4 × 2.4 arcsec^2 *bvizYJH* thumbnail images of potential $z \approx 8$ objects meeting our selection criteria in CANDELS GOODS-South field, ordered by *H*-band magnitude (brightest at the top).

3.1.3 Comparison to other studies

Both the 'deep' and 'wide' CANDELS observations of GOODS-S have been recently searched for *Y*-drop candidates by both Oesch et al. (2012, hereafter O12) and Yan et al. (2012, hereafter Y12), resulting in 11 and eight high-redshift galaxy candidates, respectively.

Of the 11 O12 sources, we match only three with our six candidates. Another object in our sample (GS.D-YD3) is also flagged as a *potential* candidate by O12 (CAND-2253348542) though is dismissed by O12 on the grounds of its stellar-like profile. We also match an additional two of our candidates with the 8 Y12 sources (there are no matches in common between all three candidate lists), thus all our candidates exist in either O12 or Y12.

Given the lack of agreement between the previous catalogues of *Y*-drops (O12 and Y12) with our new selection, and also the poor agreement between O12 and Y12 (there are two objects in common of which neither is in our candidate list), it is useful to examine each of the O12 and Y12 candidates in turn to identify why they were not selected by us.

Of the eight O12 sources not selected as candidates by us, two objects, CANDY-2499448181 (which is also 048 in Y12) and CANDY-2209651371, are detected at $>2\sigma$ in a single optical band (though at $<3\sigma$). One object (CANDY-2320345371) is excluded because its $(Y - J)$ colour is slightly bluer than our selection window, while a further four sources fail to meet our signal to noise ratio (S/N) > 5 criteria though do appear to be real objects (all detected at $>4\sigma$ in both *J* and *H* band). A single source (CANDY-219147298) is not matched within 0.5 arcsec of an object in our catalogue. Of the six Y12 sources not matched to our candidates, the two brightest (048 and 100) are excluded on the basis of weak (2σ–3σ) optical detections in a single band. The four remaining objects are excluded on the basis of S/N concerns (in that they fall below S/N = 5 in one or both bands); in three cases (094, 035, 043) we detect the source at $>4\sigma$ in both J_{125w} and H_{160w}, while the final object (085) is only detected at 2σ–3σ and has colours inconsistent with our selection window.

There are then two principal reasons for the Y12 and O12 objects being excluded from our candidate list; at the bright-end two objects in each study (with one in common) are excluded due to weak (2σ–3σ) optical detections in single band; while at the faint end several sources are excluded on the basis of our S/N criteria. In all but one case (Y12: 085) these objects are detected at $>4\sigma$ in both J_{125w} and H_{160w} and have observed colours consistent with our selection window. It then seems possible that some of the additional Y12 and O12 candidates are potential high-redshift star-forming galaxies. However, these objects are nevertheless excluded from the subsequent analysis of the rest-frame UV LF, as we want a robust sample. The computation of the effective volume takes into account our more conservative selection criteria, which should lead to the accurate LF being recovered.

4 DISCUSSION

4.1 The bright-end of the UV luminosity function at $z \approx 7$–9 from CANDELS

From our selection of z'- and *Y*-drops, we can recover the volume density of galaxies at $z \approx 7$ and $z \approx 8$ as a function of the rest-frame UV luminosity. The Lyman break technique does not have uniform sensitivity on the probed redshift range, so we quantify the probability of recovering a high-redshift galaxy in our survey as a function of redshift and absolute UV magnitudes, $p(M_{\rm UV}, z)$, with simulations. To perform these simulations, we add into the images a large number of fake galaxies, with properties similar to those of the observed high-redshift population (i.e. compact with half-light radii $r_{\rm hl} \approx 0.1$ arcsec, large Lyman α forest decrement of $D_A \approx 0.99$ and blue rest-frame UV colours). We then run our selection procedure and infer the probability of recovering such galaxies as a function of redshift and magnitude. From this probability, the effective survey volume $V_{\rm eff}$ can be calculated, with the same approach described in Steidel et al. (1999) and Stanway, Bunker & McMahon (2003). We assume the LF to have a Schechter (1976) profile with four fixed values for α, -1.5, -1.7, -1.9 and -2.1, as the faint end slope cannot be strongly constrained with current data. The other Schechter parameters, ϕ^* and M^*_{1600}, are determined by maximizing the Poissonian likelihood of observing a number of objects in a magnitude bin.

In Figs 5 and 6, we plot our data points at $z \approx 7$ (W11 selection window) and $z \approx 8$ (L11 selection window), respectively, against several LFs from our previous work (L11; W11) and other publications (Yan et al. 2010; Bouwens et al. 2011; O12). In the same figures, we also plot our data points obtained for the B11z and B11Y selection windows. As can be clearly seen, the number densities inferred from the different selection windows are in good agreement, within the error bars. We will therefore consider the lists of candidates obtained using the B11z and B11Y selection windows.

In Tables 5 and 6, we show the best-fitting results for the LF at redshifts $z \approx 7$ and $z \approx 8$, respectively, for each of the selections windows used. The candidates found in our previous works in the HUDF and ERS fields (L11; W11) are also included in all the LF calculations. In fitting the Schechter LF, ϕ^* and M^* are highly correlated, so we show the error ellipses (1σ and 2σ significance contours) for the $z \approx 7$ and $z \approx 8$–9 LFs in Fig. 7.

We note very good agreement at $z \approx 7$ between the best-fitting LFs obtained using the two different selection windows (W11 and B11z). These results are also in line with our previous estimates (W11).

At $z \approx 8$, the L11 selection window adds only two candidates to our previous sample of *Y*-drops. The B11Y selection yields six can-

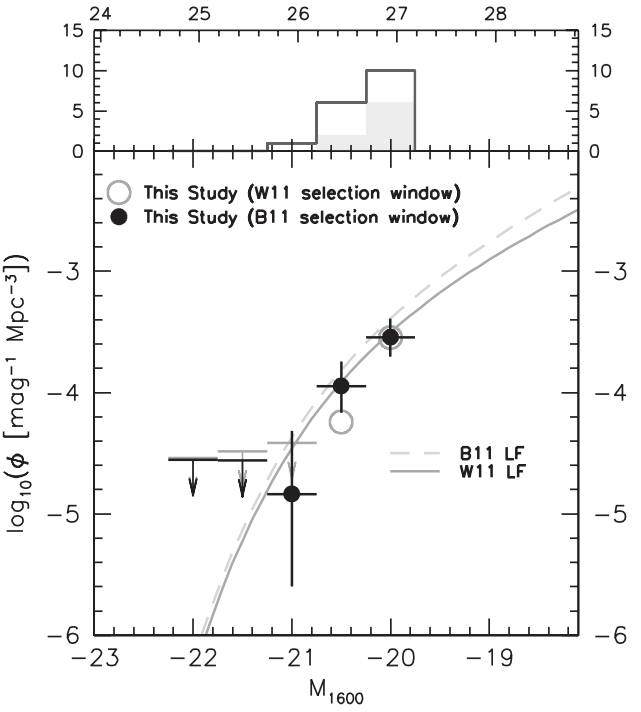

Figure 5. The luminosity distribution (top) and LF (bottom) of z'-drop selected sources at $z \approx 7$. Our data points are plotted against W11 (solid line) and Bouwens et al. (2011, dashed line) LFs. The uncertainty bars represent the 68.2 per cent Poissonian confidence interval of the number density ϕ. The upper limits denote the maximum value of the 68.2 per cent confidence interval with $n = 0$ observations. This corresponds roughly to $n = 1.84$, i.e. for an observed $n = 0$ there is a 68.2 per cent chance the true value is <1.84.

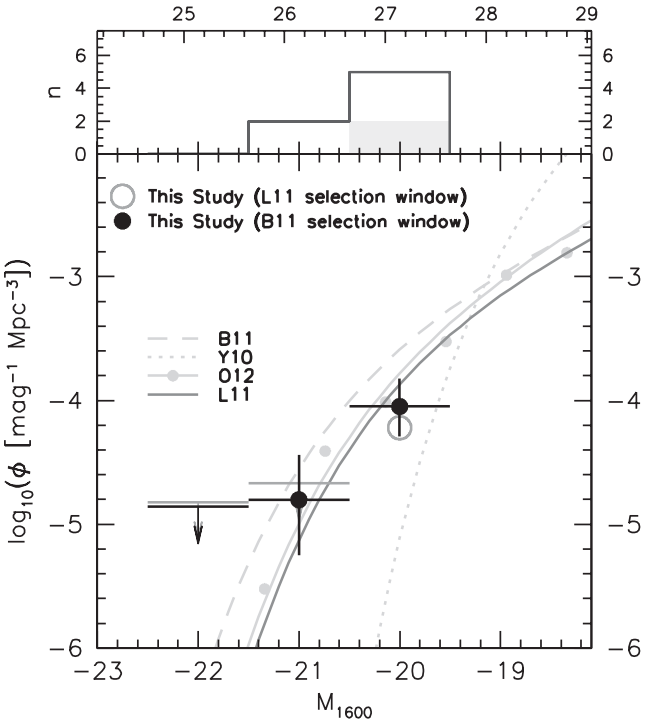

Figure 6. The luminosity distribution (top) and LF (bottom) of Y-drop selected sources at $z \approx 8$. Our data points are plotted against several LFs: L11 (solid dark line), O12 (solid light line), Bouwens et al. (2011, dashed line) and Yan et al. (2010, dotted line). The uncertainty bars represent the 68.2 per cent Poissonian confidence interval of the number density ϕ. The upper limits denote the maximum value of the 68.2 per cent confidence interval with $n = 0$ observations. This corresponds roughly to $n = 1.84$, i.e. for an observed $n = 0$ there is a 68.2 per cent chance the true value is <1.84.

didates, and combining these with our previous sample (accounting for the different effective volumes probed by the colour selections) produces LFs (Table 6) consistent with those of several previous studies L11, Bouwens et al. (2011) and O12, which indicate fainter characteristic luminosity, L^*, than at lower redshifts. However, these results at $z \approx 8$ are strongly inconsistent with the LF proposed by Yan et al. (2010) on the basis of their analysis of the HUDF, in which they claimed far more faint Y-drop galaxies than in the analyses of other groups (Bouwens at el. 2010; Bunker et al. 2010; McLure et al. 2010). As can be seen in Fig. 6, our measured number densities of Y-drops at brighter magnitudes ($M_{\rm UV} = -21$ and -20) are inconsistent by an order of magnitude or more than the expectation from the Yan et al. (2010) LF.

We now compare the star formation rate (SFR) densities obtained by integrating the $z \approx 7$ and $z \approx 8$ LFs down to various limiting magnitudes (Figs 8 and 9) to the SFR densities required for reionization from the Madau, Haardt & Rees (1999) relation:

$$\dot{\rho}_{\rm SFR} \approx \frac{0.012\,{\rm M}_\odot\,{\rm yr}^{-1}\,{\rm Mpc}^{-3}}{f_{\rm esc}} \left(\frac{1+z}{1+8.6}\right)^3 \left(\frac{\Omega_{\rm b}\,h_{70}^2}{0.0462}\right)^2 \left(\frac{C}{5}\right).$$

We have updated equation (27) of Madau et al. (1999) for a more recent concordance cosmology estimate of the baryon density from Larson et al. (2011), $\Omega_{\rm b}\,h_{100}^2 = 0.022\,622$. In the above equation, C is the clumping factor of neutral hydrogen, $C = \langle \rho_{\rm HI}^2 \rangle \langle \rho_{\rm HI} \rangle^{-2}$, whose used value in this work is 5 (Pawlik, Schaye & van Scherpenzeel 2009). $f_{\rm esc}$ is the escape fraction of ionizing photons, which is highly uncertain – we consider escape fractions as high as 100 per cent (rather implausible) and down to 10 per cent (which may be the average at $z \approx 3$ population; Nestor et al. 2011). At $z \approx 8.6$ (the av-

Table 5. The best-fitting values for M^*_{1600} and ϕ^* at $z \approx 7$ for a Schechter function assuming fixed $\alpha \in \{-1.5, -1.7, -1.9, -2.1\}$ for both the W11 (columns 2 and 3) and B11z (columns 4 and 5) selection windows.

	$z \approx 7$			
	W11		B11z	
α	M^*_{1600} (AB mag)	ϕ^* (Mpc^{-3})	M^*_{1600} (AB mag)	(Mpc^{-3})
−1.5	−19.75	0.00152	−19.75	0.00159
−1.7	−19.95	0.00110	−19.93	0.00119
−1.9	−20.19	0.00072	−20.14	0.00081
−2.1	−20.51	0.00039	−20.40	0.00049

Table 6. The best-fitting values for M^*_{1600} and ϕ^* at $z \approx 8$ for a Schechter function assuming fixed $\alpha \in \{-1.5, -1.7, -1.9, -2.1\}$ for both the L11 (columns 2 and 3) and B11Y (columns 4 and 5) selection windows.

	$z \approx 8$			
	L11		B11Y	
α	M^*_{1600} (AB mag)	ϕ^* (Mpc^{-3})	M^*_{1600} (AB mag)	(Mpc^{-3})
−1.5	−19.10	0.00143	−19.42	0.00088
−1.7	−19.23	0.00119	−19.53	0.00075
−1.9	−19.37	0.00095	−19.66	0.00060
−2.1	−19.54	0.00069	−19.80	0.00046

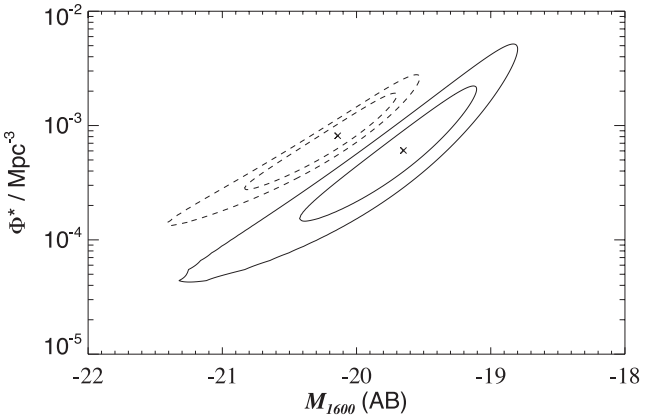

Figure 7. The likelihood contours for the LF of z'-drops (dashed lines) and *Y*-drops (solid lines), showing the correlation between the fitted M^* and ϕ^* parameters for a Schechter function fit, using our sample of galaxies from the B11 colour selection. A faint-end slope of $\alpha = -1.9$ is adopted here. The 68 per cent (inner) and 95 per cent (outer) likelihood contours are shown.The cross represents the best-fitting parameter values.

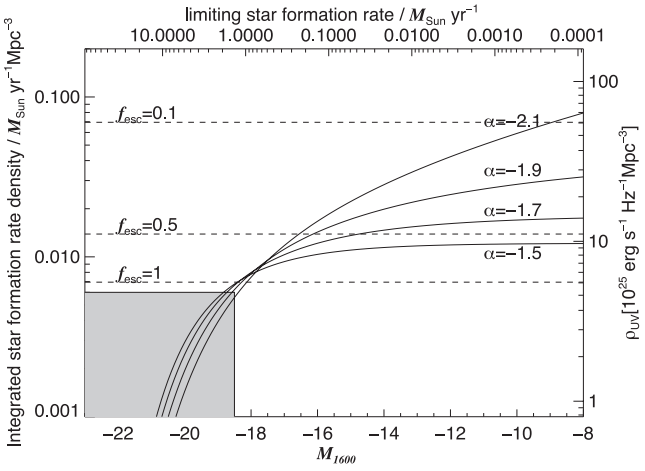

Figure 8. The solid lines are the total SFR density (left axis) or ionizing flux density (right axis) inferred from the LF fits for our z'-drop sample (for faint end slopes $\alpha = [-1.5, -1.7, -1.9, -2.1]$), integrating down to the limiting absolute magnitude in the rest-frame UV shown on the lower *x*-axis (in AB magnitudes); the upper *x*-axis shows the equivalent unobscured SFR. The dashed lines show the requirement to keep the Universe ionized at $z = 7$, using the relation from Madau et al. (1999) and assuming a low clumping factor of $C = 5$. We show the requirements for escape fractions of $f_{\rm esc} = 0.1$, 0.5 and 1. Where the solid lines cross the dashed lines, reionzation can be achieved. The shaded region is where the current deepest observations probe (the HUDF).

erage redshift of the *Y*-drops), reionization cannot be achieved with the observed LFs unless the slope is $\alpha = -1.9$ or steeper, even if the escape fraction is 100 per cent. However, a steeper faint end slope, an even lower IGM clumping factor, and a low-metallicity population (or a top-heavy IMF) might still provide sufficient photons for star-forming galaxies to reionize the Universe (see L11).

5 CONCLUSIONS

In this paper, we present a list of candidate high-redshift star-forming galaxies identified with the Lyman break technique using *HST*/WFC3 near-infrared data within the CANDELS programme.

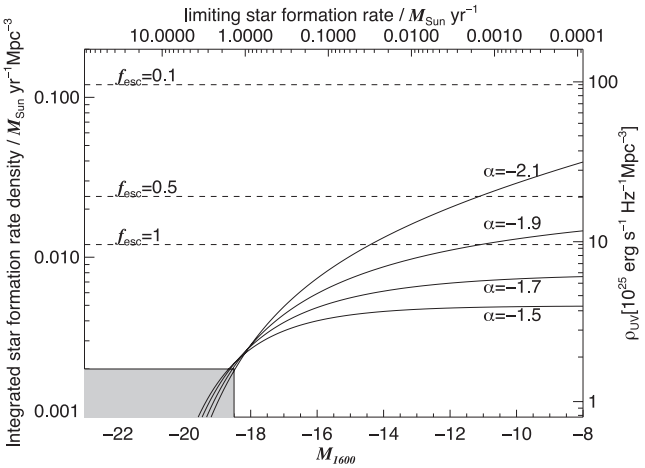

Figure 9. The solid lines are the total SFR density (left axis) or ionizing flux density (right axis) inferred from the LF fits for our *Y*-drop sample (for faint end slopes $\alpha = [-1.5, -1.7, -1.9, -2.1]$), integrating down to the limiting absolute magnitude in the rest-frame UV shown on the lower *x*-axis (in AB magnitudes); the upper *x*-axis shows the equivalent unobscured SFR. The dashed lines show the requirement to keep the Universe ionized at $z = 8.6$, using the relation from Madau et al. (1999) and assuming a low clumping factor of $C = 5$. We show the requirements for escape fractions of $f_{\rm esc} = 0.1$, 0.5 and 1. Where the solid lines cross the dashed lines, reionzation can be achieved. The shaded region is where the current deepest observations probe (the HUDF).

We have presented the first analysis of z'-drop candidate galaxies at $z \approx 7$ images with *HST*/WFC3 in the new CANDELS imaging of the GOODS-S field, building on previous work by our team (Bunker et al. 2010; Wilkins et al. 2010; W11) in the smaller HUDF and ERS fields within GOODS-S. We also use the colour selections derived by L11 and Bouwens et al. (2011) to identify candidate $z \approx 8$ *Y*-drops galaxies in this field, and compare our catalogues with those independently derived from the same CANDELS field by O12 and Y12. We treble the number of bright ($H_{\rm mag} < 27$) *Y*-drops from L11 and double the number of bright ($J_{\rm mag} < 27.2$) z'-drops from W11.

The bright high-redshift galaxy candidates we found serve to better constrain the bright end of the LF at those redshift, and may also be more amenable to spectroscopic confirmation than the fainter ones presented in various previous work on the smaller fields (HUDF and ERS). Indeed, with AB magnitudes of ≈26 (longward of the break), we could hope to detect Lyman α emission lines with rest-frame equivalent widths of a few tens of Ångstroms (typical of Lyman break galaxies at $z \sim 3$–6; e.g. Stanway et al. 2004) in ≈5 h spectroscopy with an instrument such as XSHOOTER on VLT (see Caruana et al. 2012). If spectroscopy reveals that Lyman α does not emerge at these redshifts, then our bright Lyman break galaxy sample can potentially place strong constraints on the absorption of the Gunn & Peterson (1965) damping wing (and hence the neutral fraction of hydrogen at $z \sim 8$).

We also look at the agreement with previous LFs derived from WFC3 drop-out counts, and find good agreement with those of W11 and Bouwens et al. (2011) at $z \approx 7$, and L11 and O12 at $z \approx 8$. However, our results strongly rule out the $z \approx 8$ LF proposed by Yan et al. (2010).

ACKNOWLEDGMENTS

Based on observations made with the NASA/ESA *Hubble Space Telescope*, obtained from the Data Archive at the Space Telescope

Science Institute, which is operated by the Association of Universities for Research in Astronomy, Inc., under NASA contract NAS 5-26555. These observations are associated with programmes #GO-12060, #GO-12061 and #GO-12062. We are grateful to the CANDELS team for making their data reductions public. MJJ acknowledges the support of a RCUK fellowship. SL and JC are supported by the Marie Curie Initial Training Network ELIXIR of the European Commission under contract PITN-GA-2008-214227. AJB and SMW acknowledge support from a STFC standard grant ST/G001774/1. We thank the anonymous referee for constructive comments on this paper.

NOTE ADDED IN PRESS

After submission of this paper, Grazian et al. (2012) also analysed z-drops over 40 per cent of the GOODS-S field from a subset of the CANDELS data.

REFERENCES

Beckwith S. V. W. et al., 2006, AJ, 132, 1729
Bertin E., Arnouts S., 1996, A&AS, 117, 393
Bouwens R. J. et al., 2010, ApJ, 709, L133
Bouwens R. J. et al., 2011, ApJ, 737, 90
Bradley L. D. et al., 2012, ApJ, 747, 3
Bunker A. et al., 2010, MNRAS, 409, 855
Caruana J., Bunker A. J., Wilkins S. M., Stanway E. R., Lacy M., Jarvis M. J., Lorenzoni S., Hickey S., 2012, preprint (arXiv:1208.5987)
Casertano S. et al., 2000, AJ, 120, 2747
Giavalisco M. et al., 2004, ApJ, 600, L103
Grazian A. et al., 2012, A&A, 547, 51
Grogin N. et al., 2011, ApJS, 197, 35
Gunn J. E., Peterson B. A., 1965, ApJ, 142, 1633
Knapp G. R. et al., 2004, AJ, 127, 3553
Koekemoer A. M., Fruchter A. S., Hook R. N., Hack W., 2003, in Arribas S., Koekemoer A., Whitmore B., eds, HST Calibration Workshop: Hubble after the Installation of the ACS and the NICMOS Cooling System, p. 337
Koekemoer A. M. et al., 2011, ApJS, 197, 36
Larson D. et al., 2011, ApJS, 192, 16
Leitherer C. et al., 1999, ApJS, 123, 3
Lorenzoni S., Bunker A. J., Wilkins S. M., Stanway E. R., Jarvis M. J., Caruana J., 2011, MNRAS, 414, 1455 (L11)
McLure R. J., Dunlop J. S., Cirasuolo M., Koekemoer A. M., Sabbi E., Stark D. P., Targett T. A., Ellis R. S., 2010, MNRAS, 403, 960
Madau P., Haardt F., Rees M., 1999, ApJ, 514, 648
Nestor D. B., Shapley A. E., Steidel C. C., Siana B., 2011, ApJ, 736, 18
Oesch P. A. et al., 2012, ApJ, 759, 135 (O12)
Oke J. B., Gunn J. E., 1983, ApJ, 266, 713
Pawlik A. H., Schaye J., van Scherpenzeel E., 2009, MNRAS, 394, 1812
Schechter P., 1976, ApJ, 203, 297
Schlegel D. J., Finkbeiner D. P., Davis M., 1998, ApJ, 500, 525
Stanway E. R., Bunker A. J., McMahon R. G., 2003, MNRAS, 342, 439
Stanway E. R. et al., 2004, ApJ, 604, 13
Steidel C. C., Giavalisco M., Pettini M., Dickinson M., Adelberger K. L., 1996, ApJ, 462, 17
Steidel C. C., Adelberger K. L., Giavalisco M., Dickinson M., Pettini M., 1999, ApJ, 519, 1
Trenti M. et al., 2011, ApJ, 727, 39
Wilkins S. M., Bunker A. J., Ellis R. S., Stark D., Stanway E. R., Chiu K., Lorenzoni S., Jarvis M. J., 2010, MNRAS, 403, 938
Wilkins S. M., Bunker A. J., Lorenzoni S., Caruana J., 2011a, MNRAS, 411, 23 (W11)
Wilkins S. M., Bunker A. J., Stanway E. R., Lorenzoni S., Caruana J., 2011b, MNRAS, 417, 717
Yan H., Windhorst R., Hathi N., Cohen S., Ryan R., O'Connell R., McCarthy P., 2010, Res. Astron. Astrophys., 10, 867
Yan H. et al., 2011, ApJ, 728, L22
Yan H. et al., 2012, preprint (arXiv:1112.6406) (Y12)

This paper has been typeset from a TEX/LATEX file prepared by the author.